



MIRIS: A Compact Wide-field Infrared Space Telescope

Author(s): Wonyong Han, Dae-Hee Lee, Woong-Seob Jeong, Youngsik Park, Bongkon Moon, Sung-Toon Park, Jeonghyun Pyo, Il-Joong Kim, Won-Kee Park, Dukhang Lee, Kwang-Il Seon, Uk-Won Nam, Sang-Mok Cha, Kwijong Park, Tang-Hyun Park, In-Soo Yuk, Chang Hee Ree, Ho Jin, Sun Choel Yang, Hong-Young Park, Goo-Hwan Shin, Joung-Ki Seo, Seung-Wu Rhee, Jong-Oh Park, Hyung Mok Lee, Hiroshi Murakami and Toshio Matsumoto

Source: *Publications of the Astronomical Society of the Pacific*, Vol. 126, No. 943 (September 2014), pp. 853-862

Published by: Astronomical Society of the Pacific

Stable URL: <https://www.jstor.org/stable/10.1086/678130>

Accessed: 05-05-2021 09:32 UTC

JSTOR is a not-for-profit service that helps scholars, researchers, and students discover, use, and build upon a wide range of content in a trusted digital archive. We use information technology and tools to increase productivity and facilitate new forms of scholarship. For more information about JSTOR, please contact support@jstor.org.

Your use of the JSTOR archive indicates your acceptance of the Terms & Conditions of Use, available at
<https://about.jstor.org/terms>



Astronomical Society of the Pacific is collaborating with JSTOR to digitize, preserve and extend access to *Publications of the Astronomical Society of the Pacific*

MIRIS: A Compact Wide-field Infrared Space Telescope

WONYONG HAN,^{1,2} DAE-HEE LEE,¹ WOONG-SEOB JEONG,^{1,2} YOUNGSIK PARK,¹ BONGKON MOON,¹ SUNG-JOON PARK,¹ JEONGHYUN PYO,¹ IL-JOONG KIM,¹ WON-KEE PARK,¹ DUKHANG LEE,^{1,2} KWANG-IL SEON,^{1,2} UK-WON NAM,¹ SANG-MOK CHA,¹ KWIJONG PARK,¹ JANG-HYUN PARK,¹ IN-SOO YUK,¹ CHANG HEE REE,¹ HO JIN,³ SUN CHOEL YANG,⁴ HONG-YOUNG PARK,⁵ GOO-HWAN SHIN,⁵ JOUNG-KI SEO,⁵ SEUNG-WU RHEE,⁶ JONG-OH PARK,⁶ HYUNG MOK LEE,⁷ HIROSHI MURAKAMI,⁸ AND TOSHIO MATSUMOTO^{1,8,9}

Received 2014 April 28; accepted 2014 July 13; published 2014 August 18

ABSTRACT. A compact infrared space telescope called MIRIS (Multi-purpose Infra-Red Imaging System) was developed by the Korea Astronomy and Space Science Institute (KASI), and launched onboard the *Science and Technology Satellite-3* of Korea (*STSAT-3*) in 2013 November. The main mission of MIRIS is the Paschen- α emission line survey along the Galactic plane and the cosmic infrared background (CIB) observation, particularly around the north ecliptic pole region. For these missions, a wide field of view ($3.67 \times 3.67^\circ$) with an angular resolution of $51.6''$ and wavelength coverage from $0.9 \sim 2.0 \mu\text{m}$ have been adopted for MIRIS, having optical components consisting of a 80 mm main lens and four other lenses with F/2 focal ratio optics. The opto-mechanical system was carefully designed to minimize any effects from shock during the launch process and thermal variation. Also, the telescope was designed to use a passive cooling technique to maintain the temperature around 200 K in order to reduce thermal noise. A micro Stirling cooler was used to cool down the Teledyne PICNIC infrared array to 90 K, which was equipped in a dewar with four filters for infrared passbands of *I*, *H*, and Paschen- α and a dual-band continuum line filter. MIRIS system was integrated into the *STSAT-3* as its primary payload and successfully passed required tests in the laboratory, such as thermal-vacuum, vibration, and shock tests. MIRIS is now operating in sun synchronous orbits for initial tests and has observed its first images successfully.

1. INTRODUCTION

The *Science and Technology Satellite* (*STSAT*) program of Korea was established in 1999, mainly to encourage science programs in the fields of space astronomy, space physics, and space environment. The primary payload of the first program of *STSAT* (FIMS, Far-ultraviolet Imaging Spectrograph) was developed by KASI for ultraviolet wavelength observations in collaboration with the Satellite Technology Research Center (SaTReC) of the Korea Advanced Institute of Science and Tech-

nology (KAIST) and UC Berkeley, as described in detail by Edelstein et al. (2006). The *STSAT-1* was successfully launched in 2003 and operated for two years, leading to 50 scientific papers so far. The *STSAT-3* program was also started in 2008 for infrared space observations. SaTReC was responsible for developing the satellite bus system of STSAT-3, while KASI developed the main payload MIRIS. After the successful launch in 2013 November, the *STSAT-3* is now operating its initial stage in a sun-synchronous orbit of altitude around 600 km. For two years, MIRIS will perform astronomical observations in near-infrared wavelengths of $0.9 \sim 2 \mu\text{m}$ using a 256×256 PICNIC sensor, providing a $3.67 \times 3.67^\circ$ field of view with a pixel scale of $51.6''$. The earlier system design of MIRIS during the development stage was described by Han et al. (2010), Moon et al. (2010), and Ree et al. (2010).

The science mission of MIRIS is to survey the Galactic plane in the emission line of Paschen- α ($1.88 \mu\text{m}$) and to detect the cosmic infrared background (CIB) radiation. Comparing the Paschen- α map with the H α data from ground-based surveys, we can probe the origin of the warm-ionized medium (WIM) of the Galaxy and will find the physical properties of the interstellar turbulence (Seon & Witt 2012). The CIB is thought to contain the light from the first generation stars (Pop III), and it has been found fluctuation measurement of the CIB is very

¹Korea Astronomy and Space Science Institute, Yuseoung Gu, Daejeon 305-348, Korea whan@kasi.re.kr

²Korea University of Science and Technology, Yuseoung Gu, Daejeon, 305-350, Korea.

³School of Space Research, Kyung Hee University, Yongin, 446-701, Korea.

⁴Korea Basic Science Institute, Yuseoung Gu, Daejeon, 305-806, Korea.

⁵Satellite Technology Research Center, KAIST, Yuseoung Gu, Daejeon, 305-701, Korea.

⁶Korea Aerospace Research Institute, Yuseoung Gu, Daejeon, 305-806, Korea.

⁷Astronomy Program, Department of Physics and Astronomy, Seoul National University, 151-742, Korea.

⁸Institute of Space and Astronautical Science, 3-1-1 Yoshinodai, Chuo-ku, Sagamihara, Kanagawa 252-5210, Japan.

⁹Institute of Astronomy and Astrophysics, Academia Sinica, No.1, Sec. 4, Roosevelt Rd, Taipei 10617, Taiwan.

important. Compared with previous observations (Matsumoto et al. 2011), MIRIS has shorter wavelength bands and wider survey area (10×10 square degrees) which is crucial to understand the origin of excess CIB, particularly the north and south ecliptic pole regions. We plan to subtract the foreground from the monitoring observations of both ecliptic pole regions to examine the fine features in background. More details of the science missions will be described separately by Jeong et al. (2014, in preparation). In this paper, we present the system design of the MIRIS.

2. OVERALL MISSION DESIGN AND CONSTRAINTS

The *STSAT-3 Program of Korea* was announced in 2007, and the payload RFP (request for proposal) was released as a form of open competition in all related fields of space sciences. The MIRIS proposal prepared by KASI was selected as the primary payload by the committee in the following year. In the RFP, the main payload should be specified within the requirements, for example mass (<30 kg), length (<70 cm), and power (<30 W). With these design constraints, many suggestions were discussed to make competitive science missions. Finally, it was agreed that a short focus design with a wide field of view for survey observations would be suitable with the given design conditions and budget. The other important factor was the pointing accuracy of the satellite, which is of the order of $\pm 0.13^\circ$, making it difficult to provide optimal performances for detailed imaging observations of narrow field of view with long exposure time. Therefore, two science missions for survey observations were recommended by the committee: (1) the investigation of cosmic infrared background radiation with a wide field of view ($10 \times 10^\circ$), particularly observations for the north and south ecliptic pole regions to avoid any bright infrared sources; and (2) warm ionized medium observations for $\pm 3^\circ$ area along the Galactic plane with a Paschen- α line filter, which is less affected by the scattering or extinction caused by interstellar matter.

The field of view required a short focus optical design (of order F/2) to make possible survey observations for the Galactic plane and ecliptic pole regions to be completed within two years. Simulation analysis showed that reflective optics make it very difficult to arrange a F/2 design effectively within the permitted volume of specification considering the reduced amount of light by the secondary mirror. The refractive optics rather effectively arrange for a F/2 design with an 80 mm aperture main lens for shorter focal length, which provides a 51.6" pixel scale in the case of the 40 μm pixel size of a Teledyne 256 \times 256 PICNIC sensor, giving FOV of $3.67^\circ \times 3.67^\circ$ in one frame. For the cryogenic cooling of MIRIS system, the simulation results showed that it was possible to cool down the telescope optics to 200 K by application of the passive cooling technique employing Winston cone baffle design to reject unwanted stray light from the Earth or Moon (Winston 1970). Furthermore, it was confirmed that a micro Stirling cooler can cool

TABLE 1
SPECIFICATIONS OF THE MIRIS

Parameters	Specifications
Aperture	80 mm
F-number	F/2
Effective Focal Length	160 mm
Lens Material	S-FPL53, S-TIH6, Fused Silica
Wavelength	0.9 \sim 2 μm
Filters	Broadband: I (1.076 μm), H (1.608 μm) Narrowband: Pa- α (1.876 μm) Dual-band Continuum (1.84, 1.91 μm)
Limiting Magnitude	$I : 18.6, H : 19.1$
Sensor	Teledyne PICNIC (HgCdTe)
Sensor Format	256 \times 256 pixels
Pixel Size	40 μm
Detector FOV	$3.67^\circ \times 3.67^\circ$
Pixel FOV	51.6"
Readout Noise	45 e $^-$
Telescope Temperature	180 \sim 200 K
Sensor Temperature	90 K
Compatible Orbit	595 \sim 635 km
Total Mass	29.8 kg

down the infrared sensor to 90 K from 200 K, which is the proper operational temperature of the infrared sensor. The lifetime of MIRIS was determined by the guaranteed operation time of the Stirling cooler in space environments and can provide two-year survey observations sufficiently for $\pm 3^\circ$ Galactic plane, and ecliptic pole regions. In line with this background, the specifications of MIRIS are summarized in Table 1.

3. OPTOMECHANICAL DESIGN

The optical design of MIRIS was optimized for a wide-field survey in near-infrared wavelengths. To improve the survey efficiency, an optics design with a fast F-number was investigated. We designed the MIRIS telescope with a wide-field, F/2 refractive optics using 80 mm diameter aperture. The MIRIS optics consists of five lenses (L1 \sim L5) as shown in Figure 1, among which the rear surface of the fifth lens (L5) is aspheric for optimal performance. Figure 2 shows the spot diagram in the field of view along the focal plane at different wavelengths with different colors. RMS spot size represents within 14 μm in all fields at the focal plane, which is less than 1 pixel of 40 μm in the case of a PICNIC sensor.

We have carefully chosen suitable lens materials for space environments. Three types of Ohara glasses were used, which are in the family of fluorides and are good materials for infrared optics: S-FPL53 (L1, L2, and L5), Fused Silica (L3), and S-TIH6 (L4). With the combination of these five lenses, the chromatic aberration is successfully suppressed. All lenses were also processed with an antireflection coating to increase the transmission in the wavelength band from 0.8 to 2.0 μm . Transmission curves of AR-coated lens materials were shown to be more than 98%, as described by Ree et al. (2010) with little

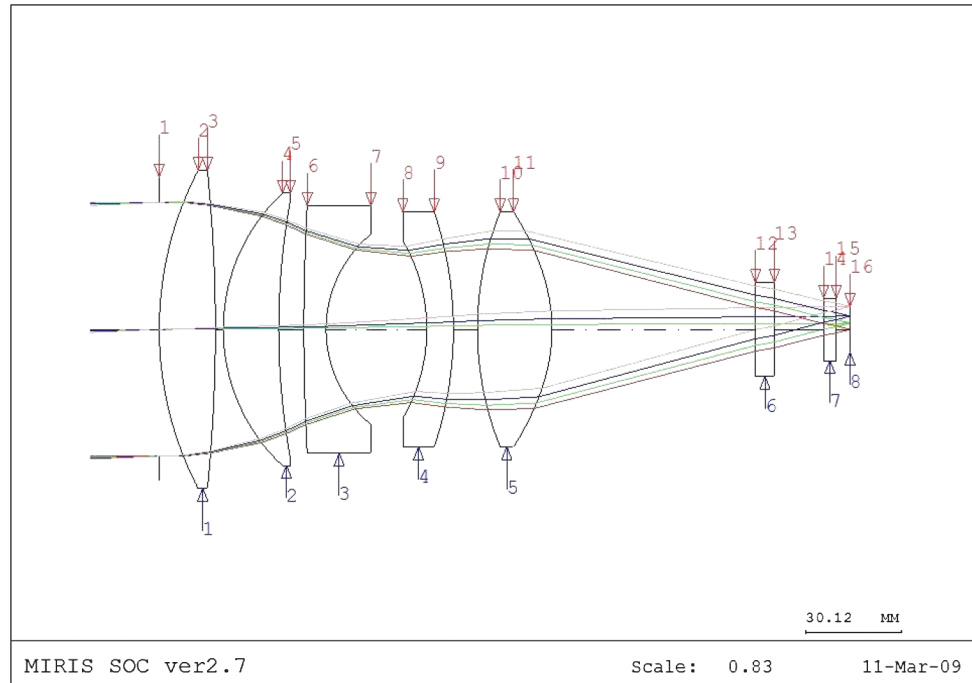
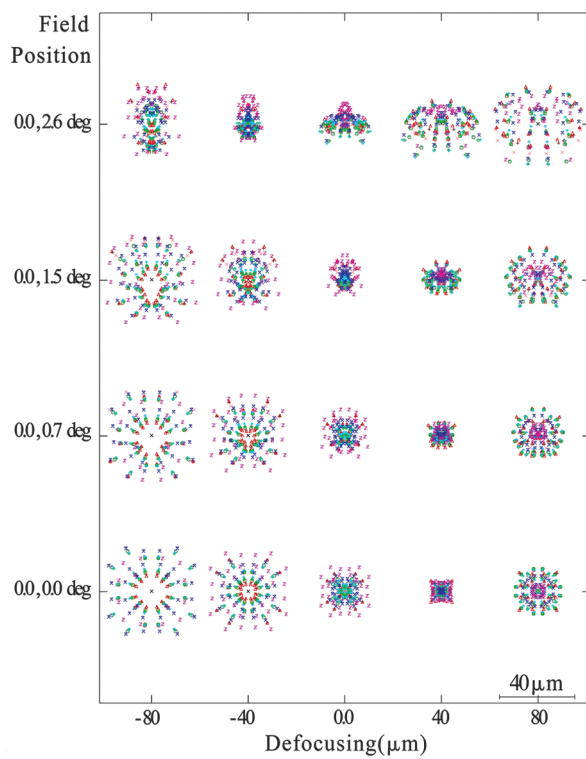


FIG. 1.—MIRIS optical layout.

FIG. 2.—Spot diagram of MIRIS along the focal plane. Different colors represent different wavelengths; for example, red for $1.9 \mu\text{m}$, green for $1.4 \mu\text{m}$ and pink for $0.8 \mu\text{m}$, respectively.

difference at cryogenic and room temperatures. A mechanical taping test and thermal cycling test were performed and passed with the coating test pieces, which were treated in the same coating process with the flight model. The total transmission of optical elements was estimated to be more than 78% in the observing wavelength region.

MIRIS optics was mounted by spacers, retainers, and flexures with no epoxy adhesive. Optomechanical parts of mounting optical lenses consist of three groups. The first group is the L1 parts accessible from the front direction. The second group is the L2 and L3 parts, also assembled from the front direction. The third group is the L4 and L5 integrated from the back direction. Figure 3 shows the final mounting layout of

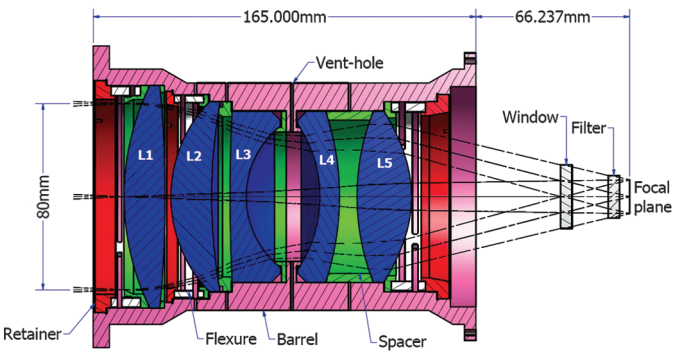


FIG. 3.—Optomechanical design and lens mounting of MIRIS. The white parts with diagonal lines are flexures, and the green parts with diagonal lines are spacers.

optomechanical parts in one barrel of the flight model. The preload of flexure was controlled based on the measurement of the spring constant individually. The lens mount was carefully designed in order to maintain the safety of the lenses during the launching conditions and cooling environments. Infrared lenses should be operated below 200 K and the lens mounting mechanism should be considered to decrease the lens contact stress during thermal contraction. Launching vibrations should also be considered for the safety of the lens optics in the small satellite. Titanium flexures were used to meet the requirements and the proper preloads were applied to each lens. Flexures can compensate for the lens stresses from thermal deformation and severe vibrations of the mounting structure. These flexures have merits that allow them to do the easy assembly and disassembly in the integration process and that can measure the spring constants easily. The final assembly of telescope optics was confirmed by measuring the Point Spread Function (PSF) size of cold and room temperatures in the focal plane.

Shock tests were made by a shock simulator equipped at KARI (Korea Aerospace Research Institute) to examine the tolerance of the spacecraft, particularly for the moment of launch. At an early stage of development with the optomechanical design described by Moon et al. (2010) for an engineering model, we experienced the serious damage of three (L1, L4, L5) among five lenses of the telescope during the shock tests. It turned out after analyzing the shock response spectrum, that the main reason for the lens damage was the resonance of natural frequency between MIRIS and flexure at 100 Hz given by acceleration of about 100 G. After failure of the shock test, the flexure preloads were increased with a margin of safety of more than 2, and the spacer mounting shape was modified in the flight model, as shown in Figure 3. After the design modification, a shock level of up to 200 G was given to the spacecraft, and we found no further damage or alteration with flight model optics of MIRIS. Before and after the shock tests, the optical performances were also confirmed by using the profiler.

For optical performance tests, MIRIS optics was designed to carry out focus tests at two phases: at room temperature and cryogenic temperature. At room temperature, we can measure the spot size at the focal plane by using the visible beam and the profiler. Then the optics was cooled down to around 200 K by a cooler of the thermal-vacuum chamber at KASI, while the dewar (including filter and sensor) was cooled down to 90 K by an internal cryogenic micro stirling cooler. Outside the chamber, we set up a collimator with an infrared light source for optimal focus tests. Once the PSF (Point Spread Function) was measured, we adjusted the shim between the camera barrel and the dewar to get the best focus. Figure 4 shows the focus test results before and after the shim adjustment indicating that the best focus is within 1 pixel, as expected.

MIRIS has four optical filters for astronomical observations and a blank filter for calibration purposes. The two broadband filters, the *I* band ($0.8 \sim 1.350 \mu\text{m}$) and *H* band ($1.15 \sim 2.05 \mu\text{m}$),

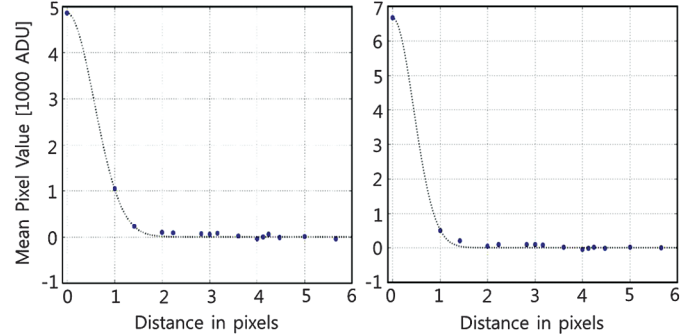


FIG. 4.—Focus test results before (left) and after (right) the shim adjustment.

will be used for the observation of CIB, and the other two narrowband filters, Paschen- α ($1.876 \mu\text{m}$) and a specially designed dual-band continuum filter, are for the Galactic plane survey. Figure 5 shows the bandpass of the MIRIS filter system.

In designing the mechanical structure of the MIRIS, the space environments for operation have to be carefully considered. The telescope should be cooled down below 200 K with a cryogenic operational temperature of the sensor at around 90 K, and has to survive launching conditions such as the shock and vibration of the spacecraft. The passive cooling concept was applied for MIRIS' optomechanical design utilizing deep space low temperature as discussed in the cases of several previous astronomical missions (Werner et al. 2004; Murakami et al. 2007; Pilbratt 2008; Nakagawa 2008; Clampin 2008). The platform temperature of the STSAT-3 spacecraft will be maintained at a common temperature, and the daily variations are expected according to the sun synchronous orbits at 600 km. Taking into account temperature control with minimum heat exchange between the spacecraft and MIRIS, we designed the mechanical configuration of MIRIS as shown in Figure 6. The structure of MIRIS consists of a radiator, a Winston cone baffle, a sunshade, a thermal-shield box, the Glass Fiber Reinforced Plastic (GFRP) pipe support, 30 layers of Multi-Layer Insulation (MLI), a cryostat, a filter-wheel, and a micro cooler.

The radiator was designed to radiate the heat load of the MIRIS by pointing to the deep space in orbits. For higher emissivity, silver-deposited Fluorinated Ethylene Propylene (FEP) was employed on an aluminum surface and the rear surface of the plate was polished to ensure higher heat transfer by increasing the contact area. To minimize the infrared radiation inflow from the telescope outside, the Winston cone baffle was designed (Winston 1970), which can reflect most of the unwanted stray light coming from the outside of the permission angle that can be controlled geometrically (Moon et al. 2010). The concept was also proved by the AKARI infrared space telescope (Bock et al. 1995), and the permission angle in case of the MIRIS is 30° . The surface of inner wall of the Winston cone baffle was processed by diamond-turning-machining, and surface treatment was finished with a gold-plating to achieve a reflectivity of 80% or more.

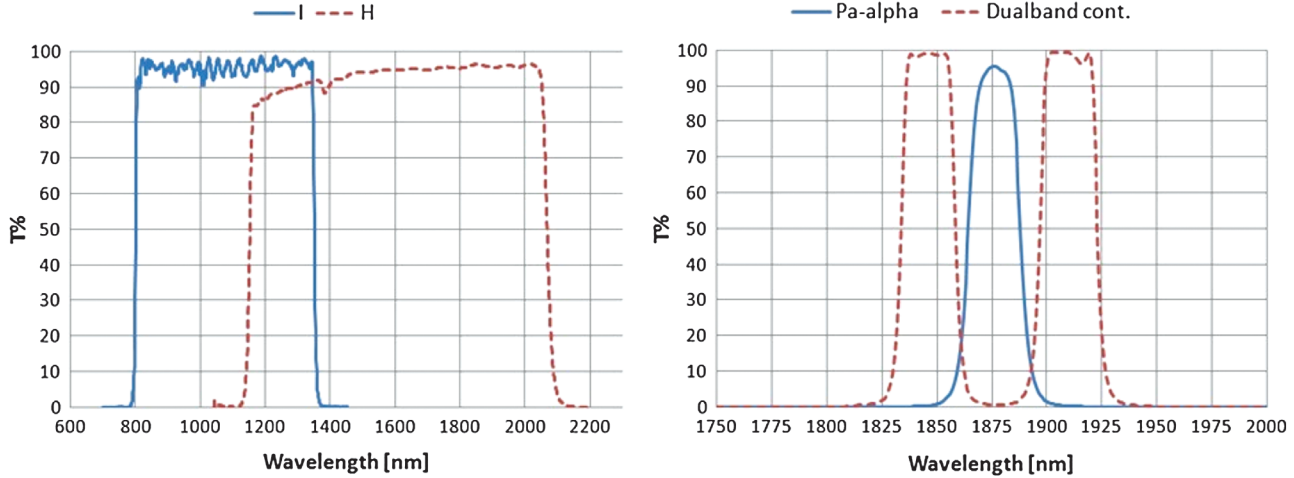


FIG. 5.—The bandpass of the MIRIS filter system for broadband I and H , and narrowband Pa- α with a dualband continuum filter.

The thermal shield box was wrapped by a 30-layer MLI to decrease thermal fluctuation of the telescope and to prevent radiation inflow from outside of the MIRIS. The 30-layer MLI makes the MIRIS components maintain low temperature by blocking the radiative heat transfer. In the case of MIRIS structure design, we also applied a 20-layer MLI for the detector module and a 30-layer MLI for telescope optics, respectively. The GFRP pipe structure was designed to support the MIRIS aboard spacecraft and to keep thermal isolation between the MLI-wrapped components. All the GFRP pipes are assembled with brackets on both sides of them, and the brackets are fixed with two snap rings and epoxy bonding. Considering the space-craft structure design, the first natural frequency was 124 Hz, which satisfied the payload requirement (above 100 Hz). Mechanical stresses also satisfied the margin of safety factor in the structure analysis (Moon et al. 2009).

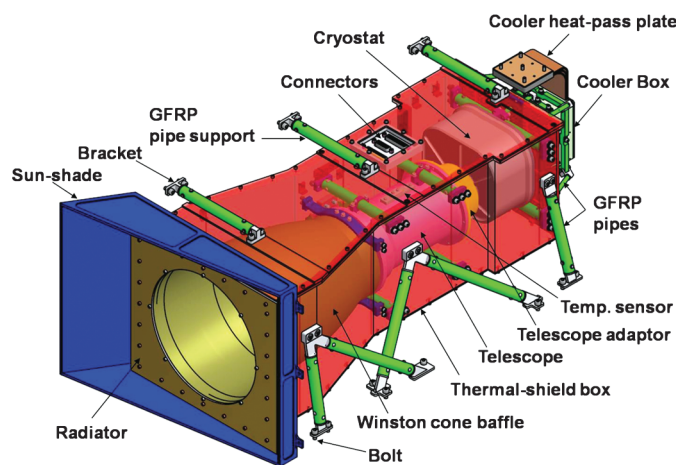


FIG. 6.—MIRIS mechanical layout.

The detector module in a cryostat was designed to be cooled down to around 90 K by a micro Stirling cooler (Ricor K508 model) at the passive-cooled space environment consuming minimum power. The cooler begins to operate when telescope temperature cools down to around 200 K and dissipates the heat load connected to the cold tip of the detector module. It takes about 10 hr to reach the required sensor temperature for observation at the laboratory after cooler operation. The MIRIS mission for survey observation requires four optical filters for the I and H bands and the Paschen- α line filter with a dual-continuum filter, plus an aluminum blank filter for dark measurements with a redundant filter. We designed a filter wheel for six filters with the size of each of them being 24 mm in diameter, considering the cryogenic operation temperature and launch environment of 10 G rms. The filter wheel is operated by a cryogenic stepping motor (model VSS25 made by Phytron) assembled with a worm gear to reduce driving load and also to prevent possible movement of the filter wheel during the launch process. The positions of the filters are detected by one mechanical switch and three magnetic sensors. Figure 7 shows the filter wheel and driving system of the flight model in MIRIS.

4. PASSIVE COOLING THERMAL ANALYSIS

In order to decrease thermal background radiation and increase the signal-to-noise ratio (S/N) of the detector, the telescope of MIRIS was designed to be cooled to below 200 K by passive cooling as described in the previous section and by Moon et al. (2010). Figure 8 shows the heat transfer diagram of MIRIS. The major heat conduction through GFRP pipes were calculated as shown in Table 2. The STSAT-3 maintains high Sun and Earth avoidance angles of more than 90° for as long as possible during each orbit by controlling the satellite's attitude. This helps MIRIS receive a minimum amount of infrared radiation from the Sun and the Earth. The avoidance angles,

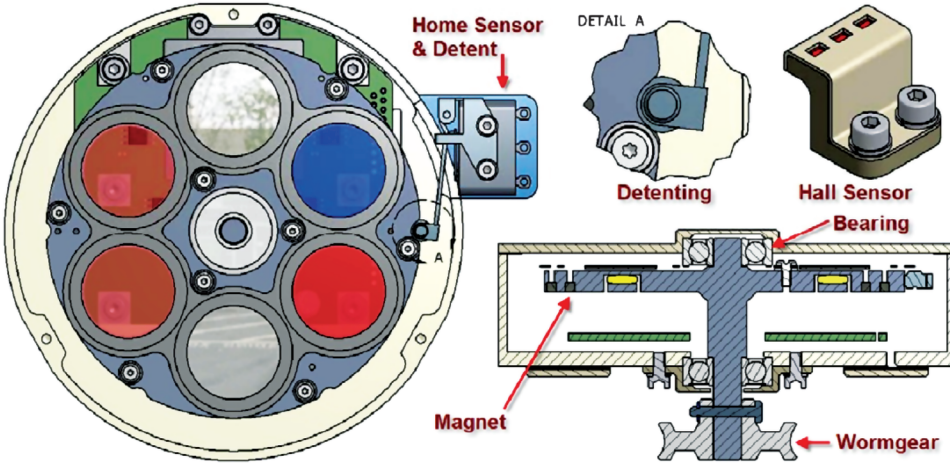


FIG. 7.—Filter-wheel and driving system overview of MIRIS.

however, are sometimes violated due to communication with the ground station or Earth observation of the secondary payloads. In spite of the violations of the avoidance angles, the thermal gain effect is canceled out by using a couple of spare orbits for passive cooling.

Before the launch of *STSAT-3*, thermal analysis was conducted to verify the passive cooling. The analysis was conducted with the NX Space Systems Thermal software. The

detailed analysis models and the results are described in Lee et al. (2012). For comparison, they used two different orbital attitudes in the thermal analysis: the hot case and the normal case. For the hot case, MIRIS points toward the direction of the normal orbit, and therefore the radiator directly receives thermal radiation from the Earth during the daytime. In the normal case, MIRIS points to deep space and avoids heat radiation from the Earth and the Sun. The results of the thermal analysis for the two cases are shown in Figure 9.

The result for the normal case can be regarded as the lower temperature limit because the analysis assumed perfect and ideal conditions for the passive cooling. The normal case, for example, assumes that the satellite has no communication with the ground station and MIRIS points to the direction in which minimum thermal radiation enters during an orbit. On the other hand, the result for the hot case can be an upper temperature limit of normal operations of MIRIS. As a result, the thermal analysis shows that the telescope of MIRIS can be cooled to below 200 K in normal operations. We also conducted a passive cooling test with the flight model (FM) of MIRIS in a vacuum chamber. This laboratory test showed that the telescope was cooled down to 200 K, and the detector was successfully cooled to 90 K by using a micro Stirling cooler.

The thermal vacuum test at the unit level of MIRIS was made several times with a thermal vacuum chamber equipped at KASI to verify the passive cooling technique. It was also necessary for the whole spacecraft to be put under a thermal vacuum test with MIRIS assembled to verify the thermal cycle at the spacecraft level. A large thermal vacuum chamber equipped at KARI was used for this test. The *STSAT-3*, integrated with MIRIS, was installed inside the chamber, and 2.5 thermal cycle tests were made. After the stabilized temperature, the MIRIS image tests were made, and we found proper operation of the system for the launch. More details for this test has been described by Han et al. (2014).

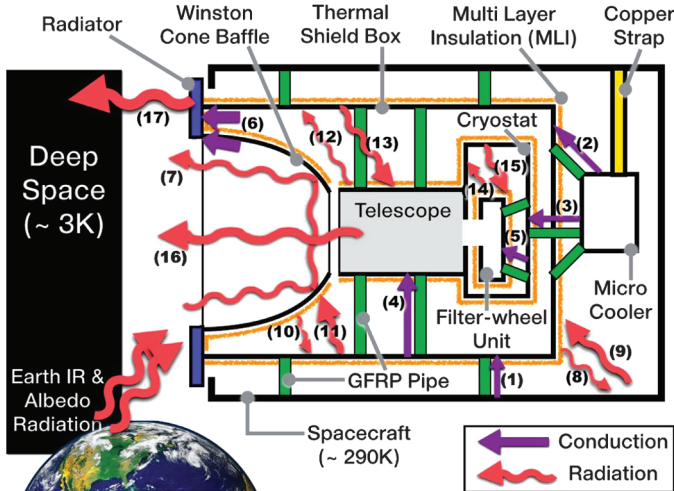


FIG. 8.—Heat transfer diagram of MIRIS. Conduction: (1) from the spacecraft to the thermal shield box (T/S box), (2) from the micro cooler to the T/S box, (3) from the micro cooler to the cryostat, (4) from the T/S box to the telescope, (5) from the cryostat to the filter-wheel unit (FWU), (6) from the T/S box and the Winston cone baffle to the radiator. Radiation: (7) unwanted stray light reflected by the Winston cone baffle, (8) from the MLI over the T/S box to the spacecraft, (10) from the MLI over the Winston cone baffle to the T/S box, (12) from the MLI over the telescope to the T/S box, (14) from the MLI over the FWU to the cryostat, (16) from the optical system of the telescope to the deep space, (17) from the radiator into the deep space. (9), (11), (13), and (15) are radiations from the opposite directions of (8), (10), (12), and (14), respectively.

TABLE 2
CALCULATED CONDUCTIVE HEAT WITH THE PATH NUMBERS DEFINED IN FIG. 8, T/S BOX:
THERMAL SHIELD BOX, FWU: FILTER-WHEEL UNIT

Path Number	Direction of Heat Transfer	Conductive Heat	Unit	Remarks
(1)	From the spacecraft to the T/S box	2.58	mW/K	Total conductance
(2)	From the micro cooler to the T/S box	575.87	mW	Generated heat load
(3)	From the micro cooler to the cryostat	51.66	mW	Generated heat load
(4)	From the T/S box to the telescope	4.60	mW/K	Total conductance
(5)	From the cryostat to the FWU	0.55	mW/K	Total conductance

5. ELECTRONICS AND INFRARED SENSOR

There are two electronics subsystems in MIRIS. The warm electronics E-Box (electronics box) is located separately from the camera system, in order to interface with the spacecraft bus. There are seven boards in the E-Box and the basic functions of them are to perform power conversion and regulation, interface data and commands with the spacecraft, monitor housekeeping data, control instrument subsystem powers and filter wheels, and clock the detector array to get the photon signals for analog-to-digital conversion. The schematic block diagram of the warm electronics and their functions were described by Han et al. (2010). Specifically, the amplifier board includes an FPGA (Field Programmable Gate Array) that contains most of the control logic and timing of driving waveforms for the array clocks, ADC control, and necessary communication signals in a single device, as shown in Figure 10.

The cold electronics is located in the dewar to interface with the IR detector array and preamplify the array outputs. We use a PICNIC 256×256 IR array by Teledyne that consists of four independent quadrants that have their own signal outputs. The multiplexer structure of the array is optimized to minimize the glow. Each quadrant contains two digital shift registers for addressing pixels in the array: a horizontal register and a vertical register. Each register requires two clocks with one being a dual edge triggered clock and one a level triggered clock. We set the

fast clock at 125 kHz to operate a pixel every 8 μ s. We use three voltage adjustments for the operation: V_{reset} , D_{sub} , and Biasgate. V_{reset} is the reset voltage that gets applied to the detectors during the reset operation, which is set to 0 V. D_{sub} is the detector substrate voltage, which is set to 0.6 V. Biasgate is used to adjust the speed and dynamic range of the unit cell source follower. With the amp gain of 6, we set biasgate voltage as 2.4 V for all quadrants to obtain a dynamic range of approximately 35000 ADU (ADC Digital Unit).

Dark noise arises from statistical variation in the number of electrons thermally generated within the array, which is independent of any photon-induced signal, but highly dependent on device temperature. Similar to photon noise, dark noise follows a Poisson relationship to dark current and is equivalent to the square-root of the number of thermal electrons generated within the image exposure time (Lee et al. 2010). We have measured the dark current and dark noise of the system by CDS (Correlated Double Sampling). With the shutter closed (and inside the black vacuum-chamber), the dark current was measured as 0.067 ADU/s. To measure the gain and readout noise of the system, we set an integration sphere attached to the window of the vacuum chamber for a mean variance test since the variance is proportional to the mean with the inclination of the inverse of gain. This standard shot noise method may yield slightly higher gain due to the interpixel capacitance of the PICNIC array (Finger et al. 2005). Figure 11 shows the measurement results of the mean-variance test, indicating gain of around $10 \text{ e}^-/\text{ADU}$ and readout noise of 45 e^- . Therefore, the calculated dark current is $\sim 0.67 \text{ e}^-/\text{s}$, which is in accord with the manufacturer's specification of $\sim 0.7 \text{ e}^-/\text{s}$ (Beletic et al. 2008).

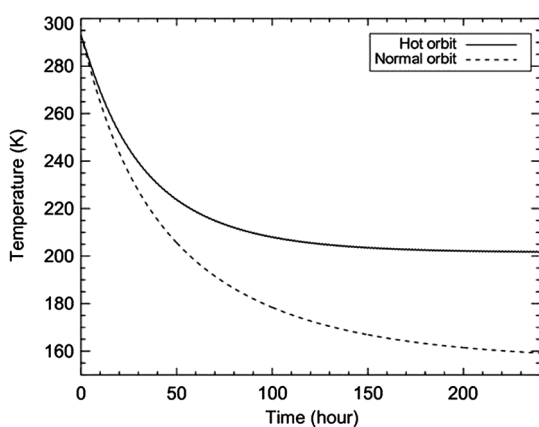


FIG. 9.—Temperature of the telescope during passive cooling for two cases of orbit attitudes.

6. DATA REDUCTION SOFTWARE

We developed Data Reduction Pipeline Software (hereafter, DRPS) for the space observation data taken by MIRIS. The software was written in Python, an open-source programming language developed and maintained by the community. It depends on Astropy (Astropy Collaboration, 2013), a community-developed core Python package for Astronomy. DRPS follows standard astronomical infrared image reduction processes.

1. Bad Pixel Masking: We identified 17 bad pixels from a detector with 256×256 dimensions. The distribution of bad

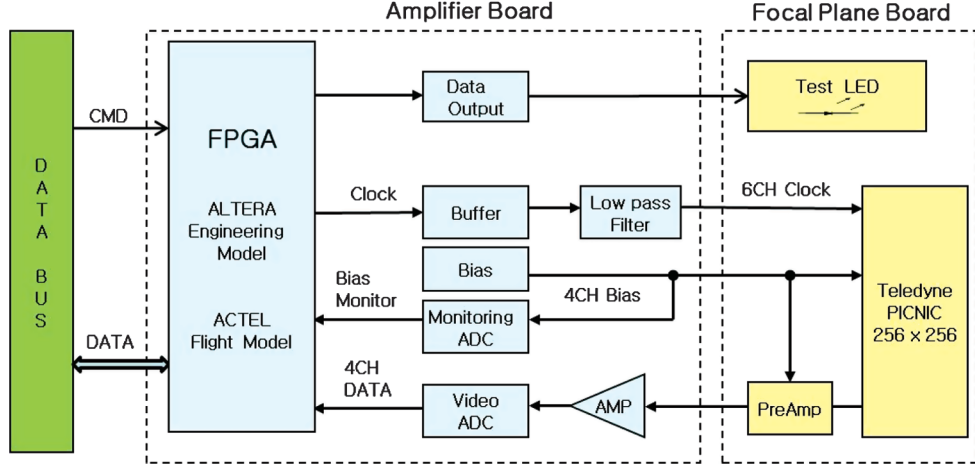


FIG. 10.—Schematic diagram of the amplifier board (AMP) and the focal plane board. The FPGA in the AMP board controls the clocks for the detector array and processes the ADC data to transmit to data bus. There are four AMP-to-ADC chains for array output signals besides the bias voltage monitoring ADCs.

pixels was almost uniform in the detector, except four clustered dead pixels. Their positions were found by examining the response curve of each pixel obtained during the ground experiment. The criteria for identification of bad pixels were either nonlinearity in a low pixel value regime or apparent odd behavior in the response curve. In the bad pixel masking process, we replace the bad pixels with not-a-number (NaN) value.

2. Linearity Correction: To examine the linearity of detector, we used images of H -band with a readout interval of 1.5 s while exposing the detector to a blackbody source until the detector saturates. From the images, we first determined the saturation value of 41,000 ADU, which is conservatively low. The pixels with values greater than 41,000 ADU were replaced with NaN and ignored. For the ground experiment images, we fitted each pixel value with a linear function of the frame numbers after reset. In the fitting, we used the images whose frame counters after reset are less than or equal to ten. The fitting result was regarded as the linearity baseline of each pixel. The experiment measurements were compared with values expected from the

baseline and the ratios were fitted with a fourth order polynomial of measured value. We correct the linearity by dividing each pixel value with the polynomial. Figure 12 compares the deviation of pixel values from linearity before and after the correction. In Figure 12, the deviation from linearity before correction for low pixel values are due to the reset anomaly. It is also corrected by the polynomial for linearity correction.

3. Differentiation: The detector collects the electrons, reads their count at specified intervals, and removes them when the reset is commanded. The nominal reset interval is 10 frames. We take the difference of two sequential frames to get the brightness per exposure time because each pixel accumulates the readout value in the frames between two resets; in this

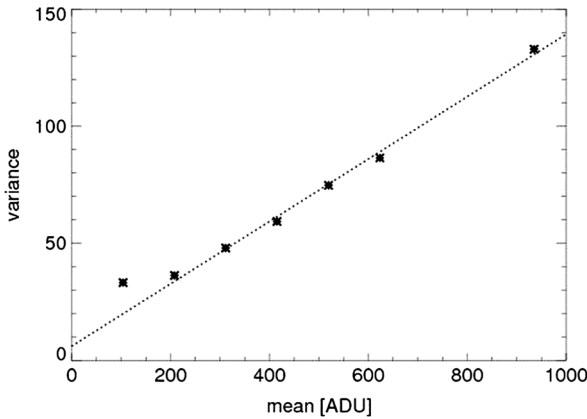


FIG. 11.—Mean-variance test result of the MIRIS detector system.

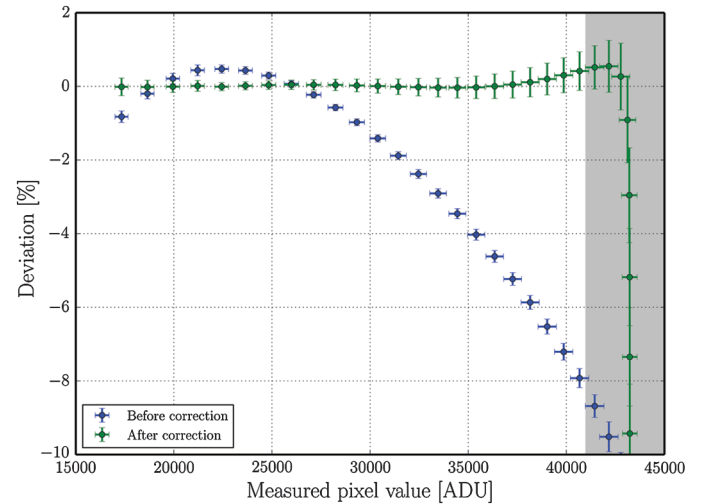


FIG. 12.—Deviation of measured pixel values from linearity before (blue) and after (green) the linearity correction. Each point shows the averages of pixel values and deviations from a single frame, while the error bars show the standard deviations. The shaded region means the pixel values are larger than the saturation of 41,000 ADU.

process, the reset frames (every eleventh frame when the reset interval is 10) and the frames just after the resets are dropped.

4. Flat-field Correction: From the flat images obtained with the blackbody source, we derived the flat-field correction images. After the procedures explained above, the flat images of each band are stacked by a median and then normalized. In this process, each image is divided by the corresponding correction image. Due to the incompleteness of the ground blackbody source, however, the correction images will be revised using the on-orbit space images.

5. Astrometry Correction: Basically, the coordinates and orientation of each image are calculated from the attitude information of the satellite's Attitude and Orbit Control System (AOCS), whose accuracy is limited. To improve the accuracy, we correct the astrometric information of each image using SExtractor (Bertin & Arnouts 1996) and Astrometry.net software packages (Lang et al. 2010). We first extract sources in the image with SExtractor. The criterion of source extraction is that more than 5 bright pixels are clustered. A pixel is considered to be bright if its value is 5 times higher than the background variation. We select the criteria more stringently than the default setting because the field of view of the image is wide and there are too many stars in the image. From the source list generated by SExtractor, Astrometry.net codes an asterism formed by four stars into a four-number hash. The hash is compared to the indices of hash codes generated from the USNO-B catalog to compute the candidate sets of pointing, scale, and orientation of the image. The final astrometric information is determined by checking whether the stars in the image exist in the catalog. The details of the algorithm implemented in Astrometry.net software are described in Lang et al. (2010).

6. Image Stacking: From each pointed observation, we obtain about 190 images in the nominal observation strategy where the sensor readout interval is 2 s, and the total exposure time is

8 minutes. Those images are stacked and mosaicked with the Montage toolkit through montage-wrapper, an affiliated package of Astropy. We manually generate the FITS header for stacked image to cover the whole field-of-view, to preserve the original spatial resolution ($\sim 52''$), and to align the final image along the equatorial coordinates. Montage reprojects each image according to the provided FITS header, and the pixels with NaN value are excluded during the reprojection. Because Montage weighs value of a pixel with its reprojected area overlapping with a pixel of an output image, missed pixels do not make holes after the reprojection unless they occupy a significant fraction of the input image. The reprojected images are coadded by taking the median, which automatically removes the anomalous values by cosmic ray hits.

7. FIRST LIGHT AND SUMMARY

MIRIS was integrated with STSAT-3 and was moved to Yasny launch base, Russia, in 2013 October. At the launch base, functional tests of MIRIS were made including a simulated observation process, and it was confirmed that all functions were operating as expected. After the assembly with the Dnepr Rocket, STSAT-3 was launched successfully on 2013 November 21 with other satellites. STSAT-3 settled into sun synchronous orbits in several days with an altitude of approximately 600 km, and communications were regularly made between the ground station and MIRIS with other secondary payloads. We made a series of on-orbit tests of MIRIS during the verification period and found that all functions, including passive cooling, were working as expected.

The MIRIS telescope was cooled down to around 200 K at sun synchronous orbits by the passive cooling process, and the temperature of the PICNIC IR detector was also successfully cooled down with the cooler to around 90 K, which is the proper

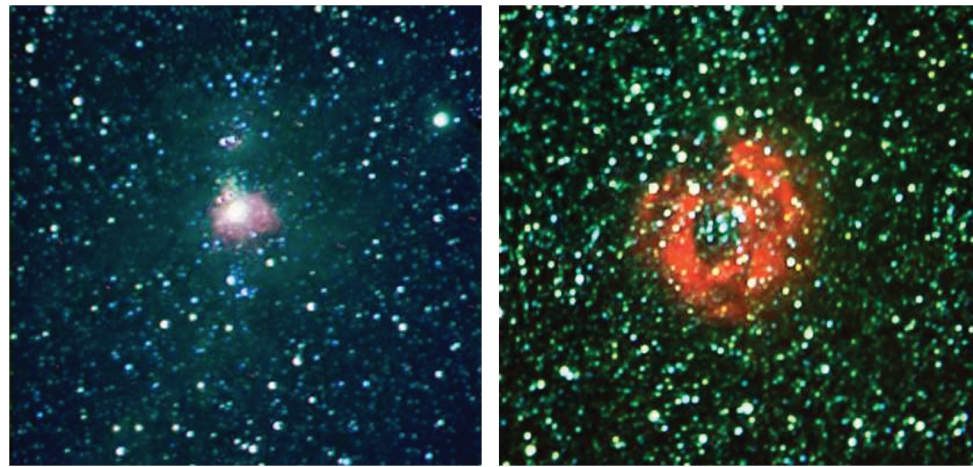


FIG. 13.—The first image from MIRIS: the left image is M42 (Orion Nebula) and the right is the Rosette Nebula. These images were composed of three filter images of I and H , and Paschen- α , mainly for functional test purposes without a calibration process.

observational temperature range. It took approximately nine hr to reach 90 K from 200 K after cooler operation in the space environment. The first light observations were made for M42 (Orion Nebula) and Rosette Nebula, as shown in Figure 13. These images were composed of three filter images of I , H and Paschen- α , mainly for functional test purposes without any proper calibration process. After initial operation for the verification period of STSAT-3, MIRIS will perform its primary science missions of (1) mapping of the Galactic plane with Paschen- α line ($1.88 \mu\text{m}$) for the study of warm interstellar medium and (2) measuring large angular fluctuations of cosmic

near infrared background radiation with I ($1.05 \mu\text{m}$) and H ($1.6 \mu\text{m}$) bands to identify the origin of these fluctuations.

We would like to thank the staff of KASI, SaTReC, and KARI for their contributions. We also appreciate the support of the ISAS/JAXA staff as well as Genesia, Co., Japan. This work was supported by a Korea Research Foundation (KRF) grant funded by the Korean government (Ministry of Science, ICT & Future Planning, No. 2011-0019041 and No. 2014034746), and also by ISAS/JAXA.

REFERENCES

- Astropy Collaboration 2013, A&A, 558, A 33
 Beletic, J. W., Blank, R., et al. 2008, Proc. SPIE, 33, 538
 Bertin, E., & Arnouts, S. 1996, A&AS, 317, 393
 Bock, J. J., Lange, A. E., Matsuhara, H., Matsumoto, T., Onaka, T., & Sato, S. 1995, Appl. Optics, 34, 2268
 Clampin, M. 2008, Proc. SPIE, 7010, 70100L-1
 Edelstein, J., Min, K.-W., Han, W., et al. 2006, ApJL, 644, L 153
 Finger, G., Dorn, R. J., Meyer, M., et al. 2005, Exp. Astron., 19, 135
 Han, W., Lee, D.-H., Park, Y., et al. 2010, Proc. SPIE, 7731, 77311W-1
 ———. 2014, End Item Data Package Documents for STSAT-3 Development, Korea Astronomy and Space Science Institute
 Lang, D., Hogg, D. W., Mierle, K., Blanton, M., & Roweis, S. 2010, ApJ, 139, 1782
 Lee, D., Han, W., Moon, B., Park, Y., Jeong, W.-S., et al. 2012, J. Astron. & Space Sci., 29, 305
 Lee, D.-H., Kim, M. G., Tsumura, K., Zemcov, M., Nam, U. W., et al. 2010, J. Astron. & Space Sci., 27, 401
 Matsumoto, T., Seo, H. J., Jeong, W.-S., et al. 2011, ApJ, 742, 124
 Moon, B., Jeong, W.-S., Cha, S., et al. 2009, Publ. Korean Astron. Soc., 24, 53
 ———. 2010, Proc. SPIE, 7731, 77311Y-1
 Murakami, H., Baba, H., & Barthel, P. 2007, PASJ, 59, S 369
 Nakagawa, T. SPICA Working Group 2008, Proc. SPIE, 7010, 70100H-1
 Pilbratt, G. L. 2008, Proc. SPIE, 7010, 701002
 Ree, C. H., Park, S.-J., Moon, B., et al. 2010, Proc. SPIE, 7731, 77311X-1
 Seon, K.-I., & Witt, A. N. 2012, ApJ, 758, 109
 Werner, M. W., Roellig, T. L., Low, F. J., et al. 2004, ApJS, 154, 1
 Winston, R. 1970, J. Opt. Soc. Am., 60, 245